Exp Fluids (2016) 57:92
DOI 10.1007/s00348-016-2177-x

RESEARCH ARTICLE

Reattachment heating upstream of short compression ramps in hypersonic flow

David Estruch-Samper[1]

Received: 1 November 2015 / Revised: 25 April 2016 / Accepted: 26 April 2016 / Published online: 12 May 2016

Abstract Hypersonic shock-wave/boundary-layer interactions with separation induce unsteady thermal loads of particularly high intensity in flow reattachment regions. Building on earlier semi-empirical correlations, the maximum heat transfer rates upstream of short compression ramp obstacles of angles $15° \leqslant \theta \leqslant 135°$ are here discretised based on time-dependent experimental measurements to develop insight into their transient nature ($M_e = 8.2$–12.3, $Re_h = 0.17 \times 10^5$–0.47×10^5). Interactions with an incoming laminar boundary layer experience transition at separation, with heat transfer oscillating between laminar and turbulent levels exceeding slightly those in fully turbulent interactions. Peak heat transfer rates are strongly influenced by the stagnation of the flow upon reattachment close ahead of obstacles and increase with ramp angle all the way up to $\theta = 135°$, whereby rates well over two orders of magnitude above the undisturbed laminar levels are intermittently measured ($q'_{\max} > 10^2 q_{u,L}$). Bearing in mind the varying degrees of strength in the competing effect between the inviscid and viscous terms—namely the square of the hypersonic similarity parameter $(M\theta)^2$ for strong interactions and the viscous interaction parameter $\bar{\chi}$ (primarily a function of Re and M)—the two physical factors that appear to most globally encompass the effects of peak heating for blunt ramps ($\theta \geqslant 45°$) are deflection angle and stagnation heat transfer, so that this may be fundamentally expressed as $q'_{\max} \propto q_{o,2D}\ \theta^2$ with further parameters in turn influencing the interaction to a lesser extent. The dominant effect of deflection angle is restricted to short obstacle heights, where the rapid expansion at the top edge of the obstacle influences the relaxation region just downstream of reattachment and leads to an upstream displacement of the separation front. The extreme heating rates result from the strengthening of the reattaching shear layer with the increase in separation length for higher deflection angle.

1 Introduction

The shock-wave/boundary-layer interaction (SBLI) induced by a compression ramp has been widely documented experimentally and, together with the impinging shock interaction, is one of the preferred canonical configurations for numerical validation in compressible flow studies (Babinsky and Harvey 2014). Interactions whereby the adverse pressure gradient is sufficiently strong so as to induce boundary layer separation are particularly complex and typically present large-scale unsteadiness (Dolling 2001; Dupont et al. 2005). At high Mach numbers, surface heat transfer rates can be extremely high and often become of primary concern in practical applications involving hypersonic flight (e.g. Schlamp et al. 2007; Knight and Longo 2012).

Surface heat transfer is highly sensitive to the state of the boundary layer and poses a challenging problem for numerical predictions, thus comprising a sensitive validation benchmark (Gnoffo et al. 2013). Noting that heat transfer measurements on SBLIs are relatively limited, a selection of pertinent experimental studies for numerical validation purposes was recently carried out by Marvin et al. (2013) under the framework of fundamental hypersonics and re-entry work. Different forms of canonical SBLIs included: two-dimensional (2D) ramp interactions at Mach 8.2, 9.2 and 11.3 (Coleman and Stollery 1972; Holden 2014), 2D

✉ David Estruch-Samper
mpedavid@nus.edu.sg

[1] Department of Mechanical Engineering, National University of Singapore, Singapore 117575, Singapore

impinging shock interactions at Mach 8.2 and 11.4 (Kussoy and Horstman 1991; Holden 2014) and axisymmetric cylinder/flare and cylinder/cowl interactions at Mach 7.1 and 8.9 (Kussoy and Horstman 1991; Murray et al. 2013), as later referred to in Sect. 3.

The present study concerns SBLIs induced by finite-span compression ramp obstacles of semi-infinite length, height of the order of the boundary layer thickness and deflection angle ranging $15° \leqslant \theta \leqslant 135°$ (Fig. 1). These interactions are strongly three-dimensional and present similar features to more commonly investigated interactions such as those induced by blunt fins (Jones 1964; Neumann and Hayes 1981), cylindrical obstacles in hypersonic flow (Hung and Patel 1984; Nestler 1985; Tang and Yu 1992; Avallone et al. 2015) and other specific protuberances (Neumann and Freeman 2012; Kumar and Reddy 2013, 2014), which generally involve the formation of a primary horseshoe vortex upon separation and its interaction with the resulting shock structure as it stretches around the obstacle. This study continues from that in Estruch-Samper et al. (2010), where semi-empirical correlations of the average heat transfer in the 'hot spot' region were derived based on common non-dimensional terms (Mach, Reynolds and Stanton numbers). An inherent limitation of correlations of this nature lies in the fact that they are restricted by their respective datasets (test conditions, geometries, methodology, etc.) and often exhibit different heat transfer trends, e.g. with Mach number captured in forms $q \propto M^{-0.5}$, M^1, $M^{1.5}$ and $M^{1.8}$ in some of the references above. A similar effect is also to be expected for Reynolds number considering the well-established diversity in trends in the wider SBLI literature. For instance, while it is most often shown to correlate positively with interaction length for low Re values (e.g. Elfstrom 1973) the trend is generally inversed at higher Re values (e.g. Settles et al. 1976) as a result of the reduced impact of viscous effects as the boundary layer gains momentum. Given the complexity of SBLIs and the inherent limitations of experimental testing, the existing database appears relatively narrow and fragmentary thus hindering a complete understanding of the associated flow mechanisms (Marvin et al. 2013; Clemens and Narayanaswamy 2014).

The need for further insight into the nature of the extreme heat transfer rates in hypersonic SBLIs prompts an assessment from a rather physics-based approach. The short ramp obstacle configuration, originally simplified to investigate the flow interference effects induced by surface protuberances on launch and re-entry vehicles, serves here as a canonical basis for the fundamental study of three-dimensional (3D) SBLIs. The geometry is further exaggerated from more common design considerations (rarely involving deflections higher than 90° in engineering design) to facilitate fundamental investigation of deflection angles up to 3 times in excess of the inviscid detached shock threshold for high Mach number flow ($\theta_D \approx 44.8°$), in turn producing a range of SBLIs rarely considered in the literature.

2 Experimental details

Experiments were conducted in a gun tunnel facility (transient, low-enthalpy) using air as the test gas and at the nominal test conditions listed in Table 1. The facility consists of a shock-compression tube connected to a convergent-divergent nozzle, which then connects to the test section and vacuum chamber. Different Reynolds number conditions Re_∞ are achieved by changing the total pressure in the driver, with the test flow in the tube set at atmospheric pressure prior to all runs. The free stream conditions used here correspond to selected nominal conditions that have been consolidated over a number of previous studies, with early calibrations dating to Needham (1963) and Mohammadian (1972), respectively, for Mach 8.2 and Mach 12.3 flows. At the datum conditions of $M_\infty = 8.2$ and $Re_\infty/m = 9.35 \times 10^6$ (highest P_o and hence Re_∞), the total

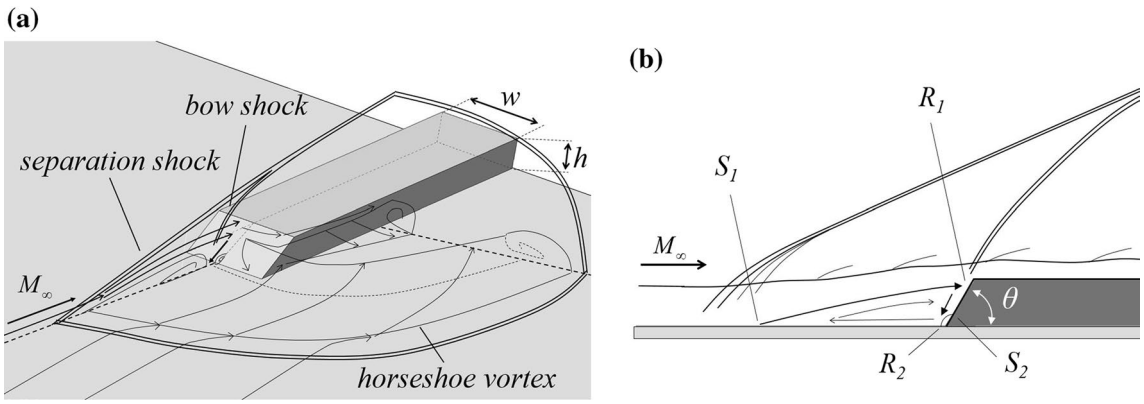

Fig. 1 Schematic of 3D SBLI induced by short ramp obstacle of height h, width w and deflection angle θ: perspective view (**a**) and side view indicating primary and secondary separation S_1, S_2 and reattachment R_1, R_2 in symmetry plane (**b**)

Table 1 Free stream flow conditions: Mach number M_∞, total pressure $P_{o,\infty}$, total temperature $T_{o,\infty}$, density ρ_∞, velocity U_∞ and unit Reynolds number Re_∞

M_∞	$P_{o,\infty}$ (MPa)	$T_{o,\infty}$ (K)	ρ_∞ (kg m^{-3})	U_∞ (m s^{-1})	Re_∞ (m^{-1})
8.2 ± 0.05	10.9 ± 1 %	1290 ± 3 %	0.0371 ± 7.1 %	1553 ± 1.6 %	$9.35 \times 10^6 \pm 7.6$ %
8.2 ± 0.05	8.2 ± 1 %	1180 ± 3 %	0.0304 ± 7.1 %	1486 ± 1.6 %	$8.06 \times 10^6 \pm 7.6$ %
8.2 ± 0.05	5.4 ± 1 %	1040 ± 3 %	0.0230 ± 7.1 %	1395 ± 1.6 %	$6.57 \times 10^6 \pm 7.7$ %
12.3 ± 0.05	10.9 ± 1 %	1290 ± 3 %	0.0054 ± 7.1 %	1584 ± 1.5 %	$3.35 \times 10^6 \pm 7.5$ %

All with wall temperature $T_w = 295\,K \pm 1.7$ %

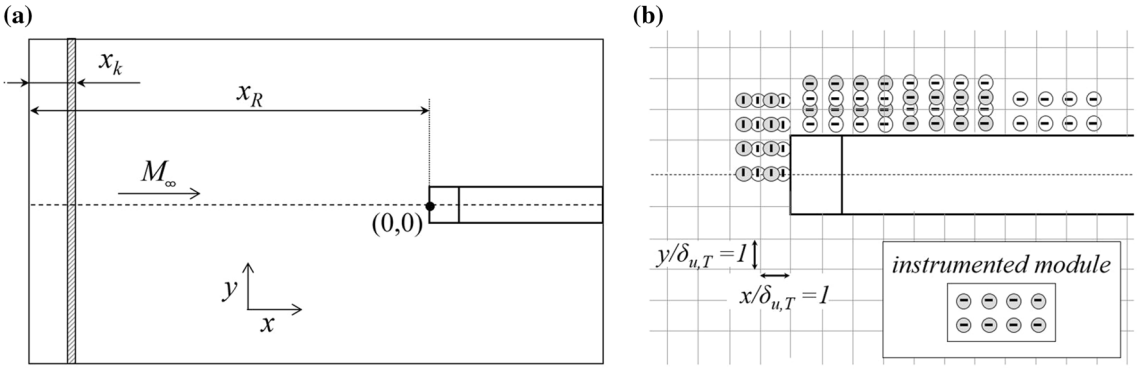

Fig. 2 Plan view schematic of test model arrangement indicating trip and reference ramp locations, x_k and x_R, and origin at the centreline of ramp obstacle leading edge (**a**); and sample of overall mapping in the vicinity of $\theta = 30°$ ramp with groups of eight sensors coloured according to instrumented module arrangement setting for different gun tunnel runs (**b**)

run duration is 31 ms and the established flow window lies between 10 and 20 ms from tunnel start. A laminar boundary layer develops naturally over the smooth flat plate, which is then tripped at $x_k = 20$ mm in some of the test cases to alter accordingly the state of the boundary layer approaching the ramp obstacles at $x_R \approx 175$ mm (Fig. 2a). At the datum test conditions, the laminar boundary layer thickness at x_R is $\delta_{u,L} = 2.5$ mm and the turbulent boundary layer thickness at the same location is $\delta_{u,T} = 5$ mm. Further details on the facility and the undisturbed flow conditions can be found in Estruch-Samper et al. (2010).

The study considers obstacles of height $h = 5$ mm and width $w = 13.5$ mm (i.e. with shallow frontal geometry $h/w < 1$), and semi-infinite length up to plate trailing edge. Ramp obstacles with deflection angles $\theta = 15°, 30°, 45°, 60°, 90°$ and $135°$ were individually tested, and the area surrounding the obstacle was mapped through combinations of test model arrangements requiring extensive experimental testing on a variety of configurations. As per Fig. 2b, 8 sensors were used at a time and fixed on an interchangeable module, with accordingly designed blanks and fixing locations, and measurements were taken along and on one side of the centreline. The sensors—supplied by RWTH Aachen University—consisted of a ceramic substrate (zirconium oxide) with sputtered nickel thin-film elements of dimensions 1.2 mm-long and 0.3 mm-wide (measurement area ~0.36 mm^2) and thickness ~0.5 μm (response time ~1 μs). They were accordingly oriented perpendicular to the direction of the highest gradients within the flow, i.e. normal to the front and sides of obstacles, with a spatial resolution of up to 2 mm.

Measurements rely on the analogue integration approach of Schultz and Jones (1973)—based on the theory of one-dimensional heat conduction—and made use of Contech analogue integrator electronics (HTA1 5R.0185) for the conversion of the voltage change associated with the temperature rise into heat transfer. The signals were low-pass-filtered at 50 kHz (Fylde 3018-F) and subsequently digitised through a National Instruments BNC-2110 DAQ data acquisition board at a sampling rate of 100 kS/s without requiring prior amplification. System gain was calibrated at $G = 2.06$ within ±2 % up to 50 kHz, and with the upper −3 dB point at 85 kHz (i.e. cutoff frequency where gain is attenuated to half the power). The time and frequency response of the system can be safely estimated to be, respectively, below 0.01 ms and well above 50 kHz (Oldfield et al. 1978), the latter corresponding to the present Nyquist frequency and assumed as the highest measurable frequency in this study.

Electrical noise was reduced to 5 mV, which translates into ~0.1 W/cm^2 or about 5 % of the minimum heat transfer measurement for undisturbed laminar flow and 0.1–0.5 % with respect to the peak heat transfer rates considered in the analysis in Sect. 3. Overall, a total combined uncertainty of ±10 % is estimated, including a ±5 % uncertainty in the calibration of the thermal properties of the gauges $(\sqrt{\rho c_p k})_g$, a ±2 % in the calibration of resistivity α_R and system error of 3 % (input voltage, measurement resolution angain calibration). Validation based on the measurement of stagnation heat transfer on a 5-mm-radius hemispherical nose finds a repeatability of $q_{o,N} = 132.6$ W/cm^2 ± 1.3 %, with similarly good agreement with theory (Fay and Riddell 1958), thus corroborating the conservative measure of the specified uncertainties (note uncertainties in Table 1 are effectively systematic).

By discretising the peak heat transfer rates based on the time-dependent signals (within frequency capabilities as shown in Sect. 3), the present work thus aims at providing further insight into the unsteady mechanisms of the interactions from a fundamental perspective.

3 Results

3.1 Time-dependent heat transfer

A basic distinction between interactions with incoming laminar and turbulent boundary layers lies in that the latter can sustain higher adverse pressure gradients and are consequently less prone to separate, with incipient angle here estimated to be $\theta_i \approx 15°$ for laminar flow and $\theta_i \approx 30°$ for turbulent flow (Needham and Stollery 1966). The heat transfer contours in the (x, y)-plane in Fig. 3 reflect the increased heating to the side of $\theta = 30°$ ramp obstacles under both laminar and turbulent upstream flow conditions; note all contours present one side of the domain with origin at ramp leading edge and at symmetry line (Fig. 2a). With a laminar incoming boundary layer, the heat transfer ahead of the ramp exceeds the base laminar level ($q_{u,L} = 1.8$ W/cm^2) as a result of the transitional state of the flow downstream of separation. The increased heating near the sides is associated with the formation of corner vortices through a similar entrainment mechanism as that described in Token (1974) for sharp fin obstacles. The reattachment of the entrained flow thus stretches along the side of the obstacle inducing a heat transfer augmentation exceeding $q/q_{u,L} = 6.5$ in laminar flow and $q/q_{u,T} = 2$ in turbulent flow, where $q_{u,T} = 5.9$ W/cm^2. Both levels are practically similar in absolute terms given the effectively turbulent state of the reattaching flow in both situations, yet with the latter inherently exhibiting a more diffuse pattern (Fig. 3b).

Time-dependent heat transfer measurements at the centreline ahead of ramps $\theta = 15°$, 30° and 45° are shown over a period of t=2 ms in Fig. 4a, b, respectively, for laminar and turbulent incoming boundary layers at $M_\infty = 8.2$ and $Re_\infty/m = 9.35 \times 10^6$ (with edge velocity $U_e \approx U_\infty$ and hence $M_e = 8.2, Re_h = 0.47 \times 10^5$). In the $\theta = 15°$ laminar case, the interaction is near incipient conditions and the heat transfer upstream remains at the undisturbed laminar level ($q/q_{u,L} \approx 1$). As deflection angle is increased to $\theta = 30°$ and 45° (Fig. 4a), the local heating exhibits increased unsteadiness as heat transfer effectively oscillates between the base laminar levels and the turbulent levels attained in the respective fully turbulent interactions in Fig. 4b (note the different scaling in terms of $q/q_{u,L}$ and $q/q_{u,T}$). Under free stream laminar conditions, transition onset takes place at the location of laminar separation upstream of the ramp and heat transfer approaches the fully turbulent level over a relatively short distance, i.e. effectively 'bypass' transition occurs. The heat transfer upstream of the $\theta = 15°$ and 30° ramps in turbulent flow (Fig. 4b) remains at the reference turbulent level $q/q_{u,T} \approx 1$ and is then amplified to $q/q_{u,T} \approx 3.5 \pm 1$ in the $\theta = 45°$ turbulent case as upstream flow separation is induced. The heat transfer contours and their respective normalised standard deviation in Fig. 5a–f show the gradual shift of the location of peak heating from the side in the lowest deflection cases towards the front as deflection angle is increased above incipient conditions ($\theta > \theta_i$).

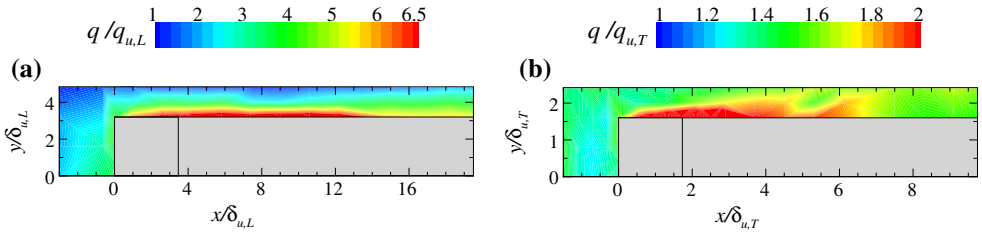

Fig. 3 Surface heat transfer contours in the (x, y)-plane for $\theta = 30°$ ramps at $M_\infty = 8.2$ and $Re_\infty/m = 9.35 \times 10^6$: with incoming laminar boundary layer (**a**) and turbulent boundary layer (**b**)

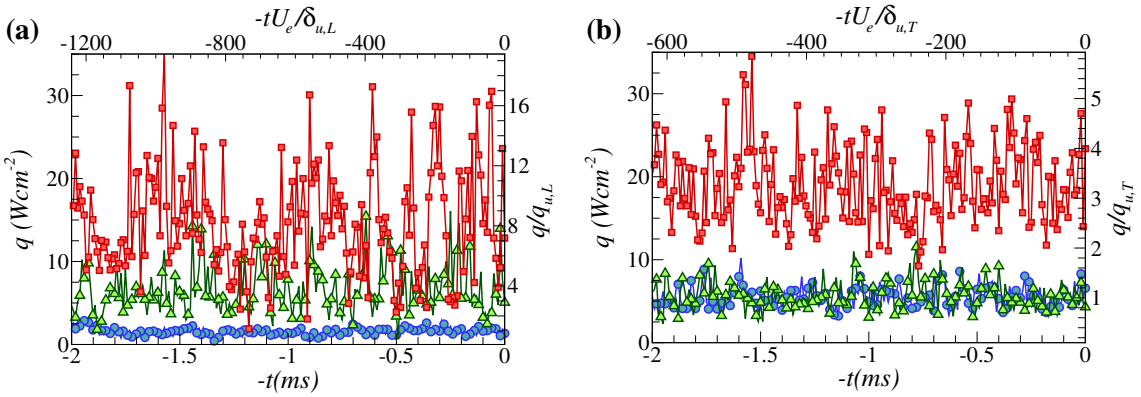

Fig. 4 Time-dependent heat transfer traces for $\theta = 15°$ (*circle symbol*), $\theta = 30°$ (*triangle symbol*) and $\theta = 45°$ (*square symbols*) ramps with incoming laminar boundary layer (**a**) and turbulent boundary layer (**b**). At $M_\infty = 8.2$ and $Re_\infty/m = 9.35 \times 10^6$, at $x = -1.5$ mm over centreline

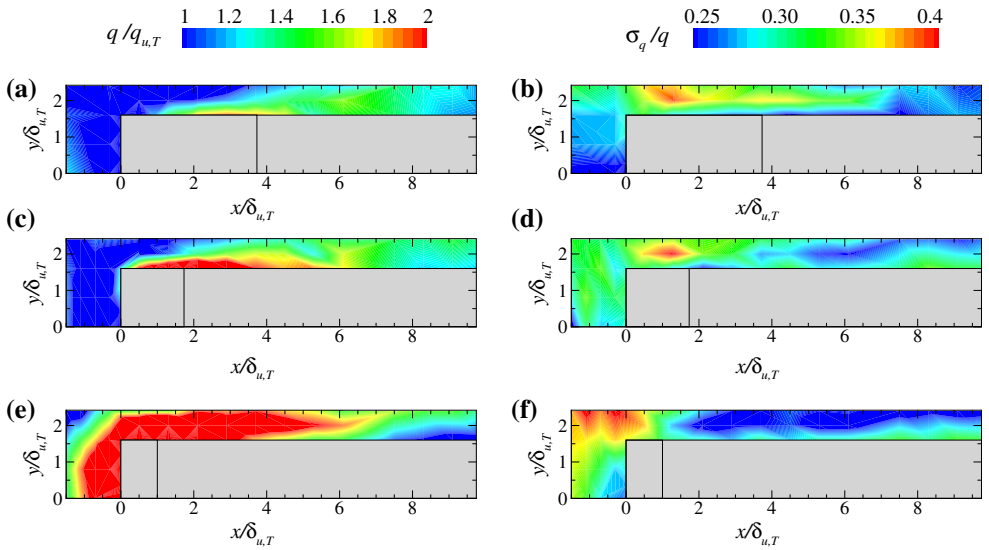

Fig. 5 Surface heat transfer contours and corresponding normalised standard deviation in the (x, y)-plane in the vicinity of protuberances at $M_\infty = 8.2$ and $Re_\infty/m = 9.35 \times 10^6$ for deflection angles: $\theta = 15°$ (**a**, **b**), $\theta = 30°$ (**c**, **d**) and $\theta = 45°$ (**e**, **f**) with incoming turbulent boundary layer. Cases correspond to those in Fig. 4b

As deflection angle is further incremented from $\theta = 45°$–$135°$ (Fig. 6), the heat transfer ahead of the obstacle increases gradually and reaches levels well over an order of magnitude higher than the undisturbed turbulent reference level $q_{u,T}$ and even two orders of magnitude higher than the laminar level $q_{u,L}$ (note the $\theta = 45°$ cases are presented again to highlight the order of magnitude increase). As a result, particularly drastic oscillations are measured just ahead of high-deflection ramps under laminar incoming flow conditions, which even exceed slightly the respective fully turbulent counterparts given the transitional state of the flow (Reshotko 2008; Schneider 2008). The increasing magnitude of the heat transfer augmentation in the area surrounding the obstacles is further evidenced in the $q/q_{u,T}$ and σ_q/q contours in Fig. 7, which reflect the unsteady nature of the reattaching flow near the leading edge, both ahead and to the side. This effect is in part inherent to the unsteadiness of the primary and secondary separation vortices (Fig. 1) and is at the same time accompanied by a gradual increase in the extent of the separation region with deflection angle.

The peak heat transfer rates along the centreline ahead of ramps are presented in Fig. 8a, where maximum 'instantaneous' heat transfer is calculated in the form $q'_{\max} = \bar{q}_{\max} + 2\sigma_q$ as a means to obtain a systematic measure of discretised peak heating levels within the time-dependent measurements and where the measurement of intermittent heat transfer gradients at the sensor location is also partly enhanced. Since the turbulent $\theta = 30°$ ramp interaction is near incipient conditions, the heat transfer

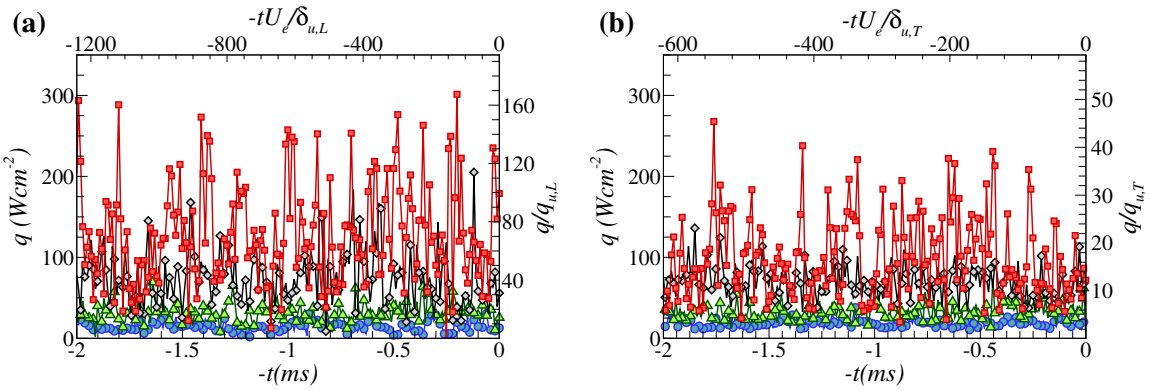

Fig. 6 Time-dependent heat transfer traces for $\theta = 45°$ (*circle symbol*), $\theta = 60°$ (*triangle symbol*), $\theta = 90°$ (*diamond symbol*) and $\theta = 135°$ (*square symbol*) ramps with incoming laminar boundary layer (**a**) and turbulent boundary layer (**b**). At $M_\infty = 8.2$ and $Re_\infty/m = 9.35 \times 10^6$, at $x = -1.5$ mm over centreline

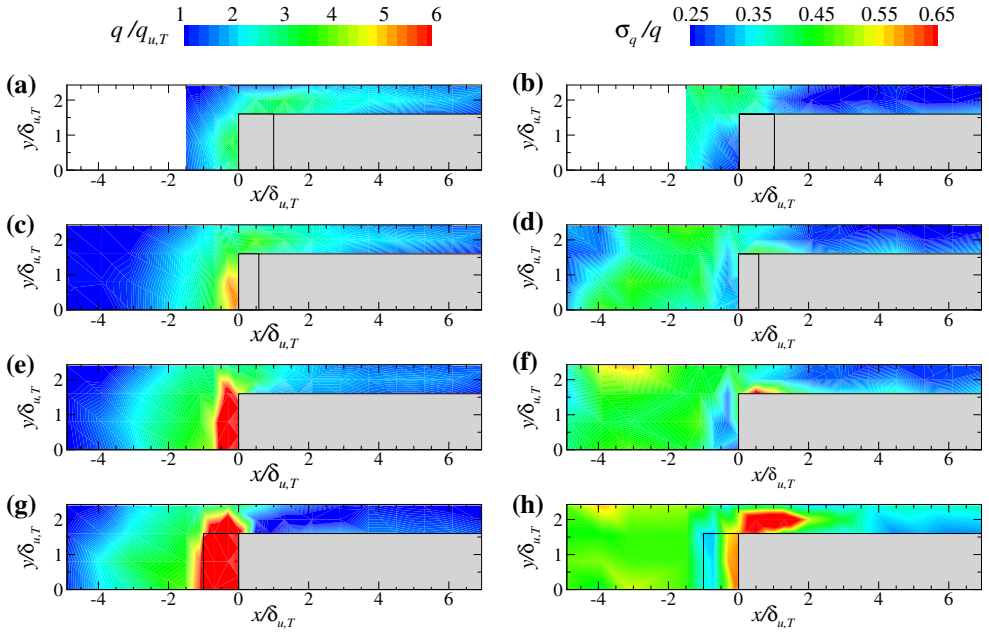

Fig. 7 Surface heat transfer contours and corresponding normalised standard deviation in the (x, y)-plane in the vicinity of protuberances at $M_\infty = 8.2$ and $Re_\infty/m = 9.35 \times 10^6$ for deflection angles: $\theta = 45°$ (**a**, **b**), $\theta = 60°$ (**c**, **d**), $\theta = 90°$ (**e**, **f**) and $\theta = 135°$ (**g**, **h**) with incoming turbulent boundary layer. Cases correspond to those in Fig. 6b

upstream remains near the undisturbed levels ($\sim q_{u,T}$). Higher deflection angles subsequently lead to a gradual heat transfer augmentation as the extent of the separation region is increased and exhibit a sharp overshoot close to the ramp. The lack of a defined plateau region despite the relatively large extent of separation (up to $L/h \approx 6$ for the $\theta = 135°$ case) is inherently due to the strong three-dimensionality of the separation and the associated horseshoe vortex and hence related to the greater lateral gradients in contrast to those for obstacles of semi-infinite width ($w >> \delta_u$). The streamwise heat transfer trends at different spanwise locations for the turbulent $\theta = 135°$ case (Fig. 8b) in fact reveal that the rapid overshoot prevails far from the centreline but still ahead of the obstacle, and goes on to drop sharply at a farther spanwise distance, with effectively no traces of it by $y/\delta_{u,T} = 2.4$ (about $\delta_{u,T}$ from lateral edge) and with particularly high lateral gradients in the vicinity of the front face. Within the wider extent of the base separation, the heat transfer augmentation maintains a similar streamwise gradient of $dq/dx \approx 0.3\mathrm{W/cm}^2$ per mm as in the lower-deflection cases in Fig. 8a, i.e. independently of downstream ramp angle and in coherence with free-interaction theory (Chapman et al. 1957). These trends are indicative of an organisation similar to that highlighted

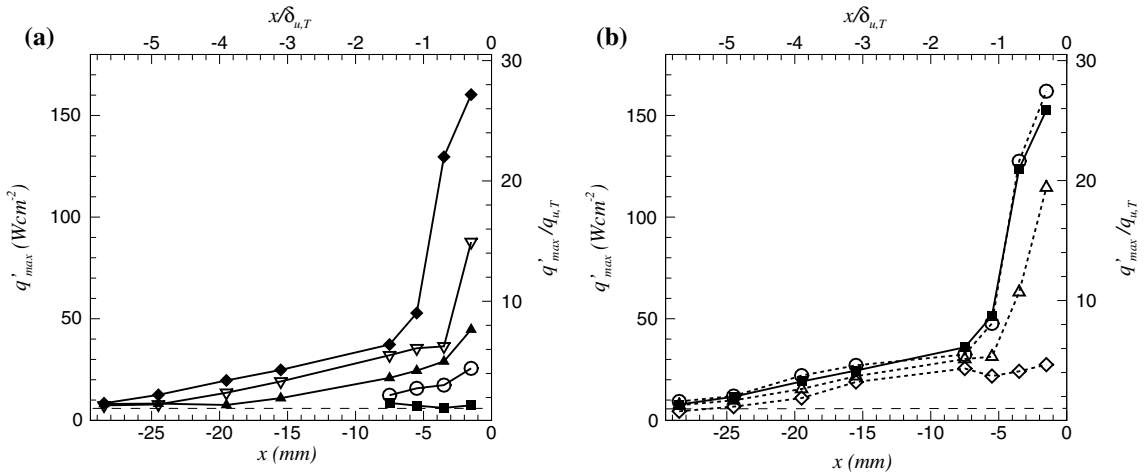

Fig. 8 Peak heat transfer rate on the centreline ahead of ramps $\theta = 30°$ (*filled square symbol*), $\theta = 45°$ (*open circle symbol*), $\theta = 60°$ (*filled triangle symbol*), $\theta = 90°$ (*open inverted triangle symbol*) and $\theta = 135°$ (*filled diamond symbol*) with incoming turbulent boundary layer (**a**); and peak heat transfer rate at locations $y/\delta_{u,T} = 0$ (*filled square symbol*), $y/\delta_{u,T} = 0.8$ (*open circle symbol*), $y/\delta_{u,T} = 1.6$ (*open triangle symbol*) and $y/\delta_{u,T} = 2.4$ (*open diamond symbol*) upstream of turbulent $\theta = 135°$ ramp (**b**). At $M_\infty = 8.2$ and $Re_\infty/m = 9.35 \times 10^6$

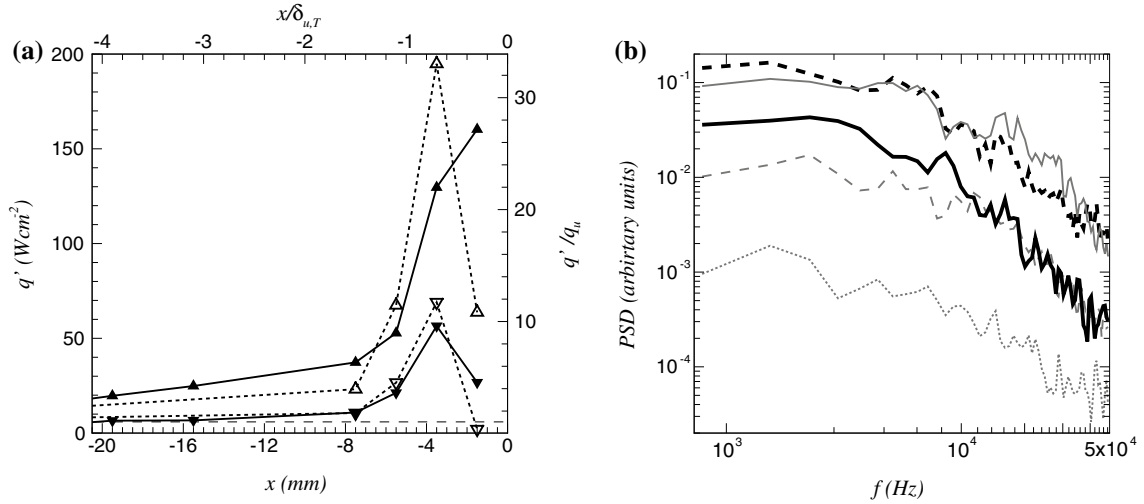

Fig. 9 Maximum and minimum heat transfer rates ahead of $\theta = 135°$ ramp with incoming laminar ($q'_{\min}$ *open inverted triangle symbol*, $q'_{\max}$ *open triangle symbol*) and turbulent boundary layer ($q'_{\min}$ *filled inverted triangle symbol*, $q'_{\max}$ *filled triangle symbol*) (**b**); and power spectral density (PSD) of signal at $x = -7.5$ mm (*grey short dashed*), $x = -5.5$ mm (*grey long dashed*), $x = -3.5$ mm (*grey solid*) and $x = -1.5$ mm (*black solid, thick*) ahead of $\theta = 135°$ obstacle in laminar flow and $x = -1.5$ mm (*black dashed, thick*) in turbulent flow. At $M_\infty = 8.2$ and $Re_\infty/m = 9.35 \times 10^6$ over centreline

for blunt fin interactions in Dolling (1982), which distinguished between the base separation region, marked by strong viscous effects, and the region closer to the obstacle where compressibility effects predominate.

A close-up to the overshoot region along the centreline for the laminar and turbulent $\theta = 135°$ obstacles is presented in Fig. 9a, including also the minimum levels ($q'_{\min} = \bar{q}_{\max} - 2\sigma_q$) to further highlight the intermittent nature of the flow. With a laminar incoming boundary layer (effectively a transitional interaction), the peak heating is located farther from the obstacle leading edge and local fluctuations vary accordingly between the $q'_{\min}$ and $q'_{\max}$ levels. In both cases, heat transfer drops intermittently to $q'_{\min}$ values of about 1–5q_u close ahead of the leading edge and exhibits oscillations of order $\pm 10 q_{u,T}$ (about $\pm 30 q_{u,L}$) at the peak heating locations. As captured in the σ_q/q contours in Fig. 7h, these large oscillations are particularly restricted to the region close to the corner, where a secondary vortex is expected. While the flow organisation may vary significantly across different

test conditions, with potentially further vortex pairs as reported for either low or high Reynolds numbers (Sedney 1973; Sedney and Kitchens 1977; Ozcan and Holt 1984), results suggest that the organisation is dominated by the main horseshoe vortex and the localised counter-rotating vortex at the corner for the present range of interactions ($0.17 \times 10^5 < Re_{\delta_u} < 0.47 \times 10^5$). The proximity of the present conditions to the $Re_{\delta_u} \approx 1 \times 10^5$ threshold—which is often regarded as an approximate limit for Reynolds number trend reversal in separation length correlations (Délery and Marvin 1986)—places the present interactions within a relatively complex regime whereby both viscous and inviscid forces play a significant role.

The unsteady behaviour of the flow within the peak heating region is further evidenced in the power spectral density (PSD) of the signals in Fig. 9b. Results reveal a predominance in low-frequency component within the overshoot region, with nearly 80 % of the energy falling within the 10^2–10^4 Hz frequency range in a broadband fashion. This effect, which is consistent with dynamic pressure measurements near the bow shock region ahead of cylindrical protuberances and blunt fins (e.g. Tang 1998; Clemens and Narayanaswamy 2014), is further enhanced at the most downstream location ($x = -1.5$ mm) for free stream laminar flow, where the secondary vortex is again subject to a transitional flow environment and thus appears particularly oscillatory (c.f. for fully turbulent flow at the same location, where low-frequency unsteadiness is mildly mitigated).

While intermittent heating effects may be dampened out across the depth of the surface and hence render $\bar{q}_{\max}$ a relevant measure to quantify the effects on the internal body structure, the evaluation of $q'_{\max}$ is here rather used as an approach for both improving fundamental understanding of the unsteady flow mechanisms and to provide further detail for validation of time-resolved numerical studies. This approach serves also to partly address limitations inherent to experimental spatial resolution and sensor location which are likely to challenge measurement of the 'true' maximum heat transfer due to the complex topology of the interactions and the high gradients close to the obstacle (Neumann and Hayes 1981).

Results for the $\theta = 90°$ obstacle are compared with existing knowledge on forward-facing step SBLIs, which comprises the best established 2D analogue configuration of relevance. Heat transfer measurements for the $\theta = 90°$ turbulent case in Fig. 10a exhibit an overshoot of up to $q'_{\max}/q_{u,T} \approx 15$ and capture the enhanced heating downstream of the detached shock within the region of flow reattachment ahead of the obstacle and spanning along the width of the compression surface (Fig. 10b, c). The origin of separation can be extrapolated to $L/h \approx 5$, which falls within the upper range of that reported in earlier studies ($4.2 < L/h < 5$ for turbulent flow as summarised in Knight and Zheltovodov 2014). The finite span of the configuration here leads to a subsequent drop in heat transfer to the side of the ramp where it reaches an almost uniform value of about $q'_{\max} \approx 2q_{u,T}$ or greater within the reattachment region stretching along the sides (Fig. 10c). This effect is associated with the formation of corner vortices and is more clearly noticed for low-deflection cases (Figs. 3, 4, 5), yet similar heating patterns are found to the side of higher deflection obstacles.

The effect of deflection angle on the upstream flow separation is thus shown to have important implications on heat transfer even for angles greater than the inviscid detached condition ($\theta > \theta_D$). This is in much contrast to compression ramp and step SBLI literature, where—as more thoroughly explained in Babinsky and Harvey (2014)—turbulent separation development is shown to be classified in the following stages according to deflection angle: I—unseparated flow below incipience conditions, II—intermittent separation, III—developing small-scale separation, IV—large-scale separation well above incipient conditions, and V—maximum-scale separation for large-deflection angles exceeding the inviscid detached shock condition θ_D (e.g. forward-facing steps and high-deflection ramps). In regime V, a detached normal shock is reported to appear ahead of the corner and the length of the separation region achieves a maximum scale which remains insensitive to further increases in deflection angle while still being dependent on ramp/step height to a certain extent (Hahn 1969; Zheltovodov 1996, 2006). Despite qualitative similarities with 2D step flows, inherent topological differences such as the fact that streamlines issuing from separation here spiral into the main recirculation focus and escape laterally (Fig. 10b) have direct implications on the shear layer development and reattachment mechanisms (Arnal and Délery 2004).

The growth in extent of the interaction with increasing deflection angle is further reflected in the schlieren images in Fig. 11a–l, where the separation shock can be seen to shift gradually farther upstream of the ramp with increasing deflection angle for both laminar and turbulent upstream flow conditions. Since fully turbulent flow poses greater resistance to separation, it results in interactions with a proportionally shorter extent, of order 4:1 with respect to interactions with an incoming boundary layer. A shock wave close ahead of the ramp is also visible in all cases shown here except for the unseparated interaction in the $\theta = 30°$ turbulent case. Well above the obstacle, the bow shock becomes shallower while the separation shock maintains its ~12° angle for all cases with upstream laminar flow (slightly higher in turbulent interactions) and with the effect of increasing ramp angle limited to inducing an upstream displacement of separation onset. The intersection between the separation shock and the bow shock takes place well above the obstacle height in all the cases and is particularly far downstream of the peak heating region under upstream

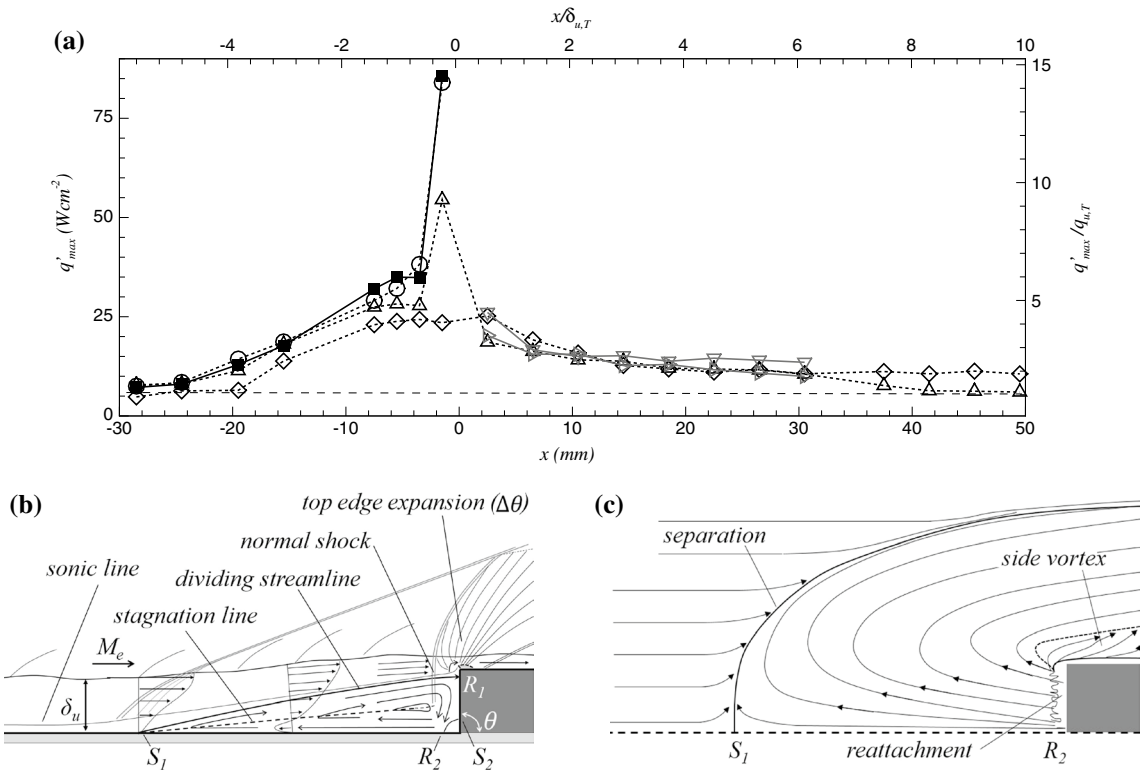

Fig. 10 Peak heat transfer rate on the centreline ahead of $\theta = 90°$ ramp at $M_\infty = 8.2$ and $Re_\infty/m = 9.35 \times 10^6$ for turbulent flow and along $y/\delta_{u,T} = 0$ (*filled square symbol*), $y/\delta_{u,T} = 0.8$ (*circle symbol*), $y/\delta_{u,T} = 1.6$ (*triangle symbol*), $y/\delta_{u,T} = 2$ (*inverted triangle symbol*), $y/\delta_{u,T} = 2.4$ (*diamond symbol*) and $y/\delta_{u,T} = 3$ (*triangle right symbol*) (**a**), together with schematics of flow in symmetry plane (**b**) and plan view of near-wall flow over separation region (**c**)

laminar flow conditions (e.g. $x/L \approx 10$ downstream of the $\theta = 90°$ obstacle's front face).

The minimum and maximum heat transfer levels ahead of ramp obstacles ($q'_{\min}$ and $q'_{\max}$) are summarised in Fig. 12a, b for all the test conditions (Table 1) together with the corresponding ratios based on undisturbed level ($q'_{\min}/q_u$ and $q'_{\max}/q_u$) in Fig. 12c, d. In fully turbulent interactions, the minimum levels $q'_{\min}$ increase slightly up to the $\theta = 90°$ cases and then decrease for $\theta = 135°$ due to the stronger oscillations associated with the larger extent of the secondary recirculation. At laminar conditions, as well as in low Re_∞ conditions with boundary layer trip, the respective $q'_{\min}/q_u$ ratios exhibit an increasing trend as the transitional state of the boundary layer is enhanced with higher deflection angle. On the other hand, the peak heat transfer rates $q'_{\max}$ increase steadily with deflection angle for all the test conditions. Transitional interactions are accordingly characterised by their higher $q'_{\max}/q_u$ ratios as an artefact of the lower reference values, which renders the trends in Fig. 12d indicative of the state of the boundary layer, i.e. whether it is effectively transitional or turbulent. Despite the varying degrees of unsteadiness across the different configurations, as particularly obvious from the $q'_{\min}$ plots, the peak heat transfer trends are fully consistent across the whole range of cases (Fig. 9a). This includes interactions for which $q'_{\max}$ does not correspond to the most downstream location and reinforces the premise that the peak heating in the vicinity of obstacles is rightly captured, as further sustained in the following sections.

3.2 Stagnation heating

As per the mechanism in Fig. 10b, the impingement of the separated shear layer upon primary reattachment on the front face of the obstacle (R_1) results in a stagnation region similar to that in hypersonic nose regions, consequently giving rise to very high heat transfer rates. While this appears more obvious for the $\theta = 90°$ obstacle, a similarly localised stagnation of the flow is also expected to some extent upon reattachment of the shear layer in

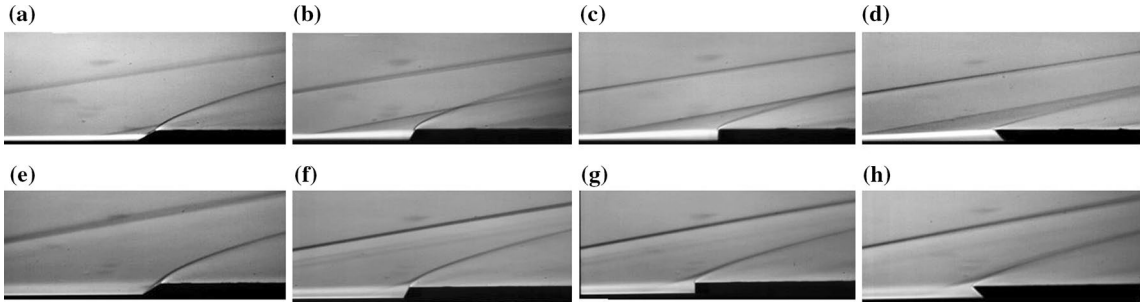

Fig. 11 Schlieren images of interactions with incoming laminar boundary layer (*top row*) and turbulent boundary layer (*bottom row*), respectively, for ramps: $\theta = 30°$ (**a**, **e**), $\theta = 60°$ (**b**, **f**), $\theta = 90°$ (**c**, **g**) and $\theta = 135°$ (**d**, **h**). Cases correspond to those in Figs. 4, 5, 6 and 7

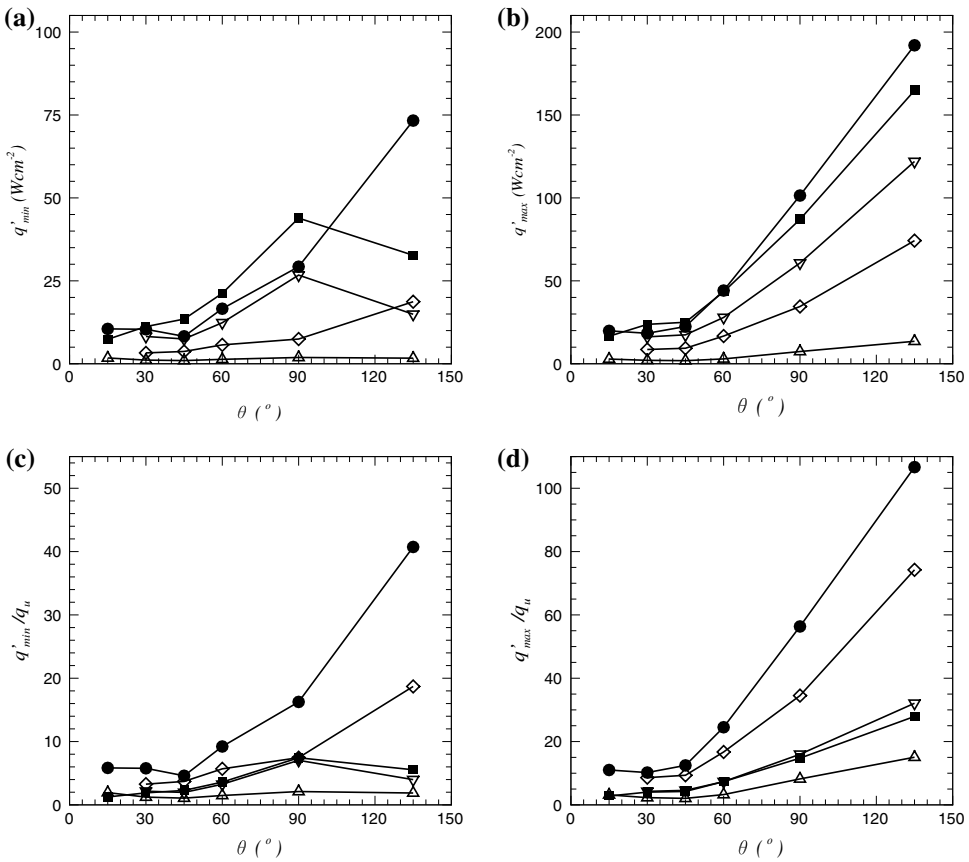

Fig. 12 Heat transfer at peak heating location ahead of ramps for different deflection angles θ: minimum heat transfer $q'_{\min}$ (**a**), peak heat transfer $q'_{\max}$ (**b**), and respective $q'_{\min}/q_u$ (**c**) and $q'_{\max}/q_u$ ratios (**d**). For test conditions in Table 1: $M_\infty = 8.2$, $Re_\infty/m = 9.35 \times 10^6$ lam. (*filled circle symbol*), $M_\infty = 8.2$, $Re_\infty/m = 9.35 \times 10^6$ turb. (*filled square symbols*), $M_\infty = 8.2$, $Re_\infty/m = 8.06 \times 10^6$ turb. (*inverted triangle symbol*), $M_\infty = 8.2$, $Re_\infty/m = 6.57 \times 10^6$ turb. (*diamond symbol*) and $M_\infty = 12.3$, $Re_\infty/m = 3.35 \times 10^6$ turb. (*triangle symbol*)

compression corner and incident shock interactions with separation (Délery and Marvin 1986), yet with the reattachment being inherently coupled to the highly complex viscous effects. Originally prompted by a need to better understand the nature of the heat transfer augmentation on the surface surrounding short protuberances—i.e. over the main vehicle surface, which is often subject to more limiting design constraints—the present analysis is in turn more particularly concerned with the maximum heating $q'_{\max}$ at the region of secondary reattachment R_2, for which extremely high heating has been shown to be induced (Sect. 3.1).

With this in mind, the complete $q'_{\max}$ dataset is first evaluated against the well-established hypersonic stagnation

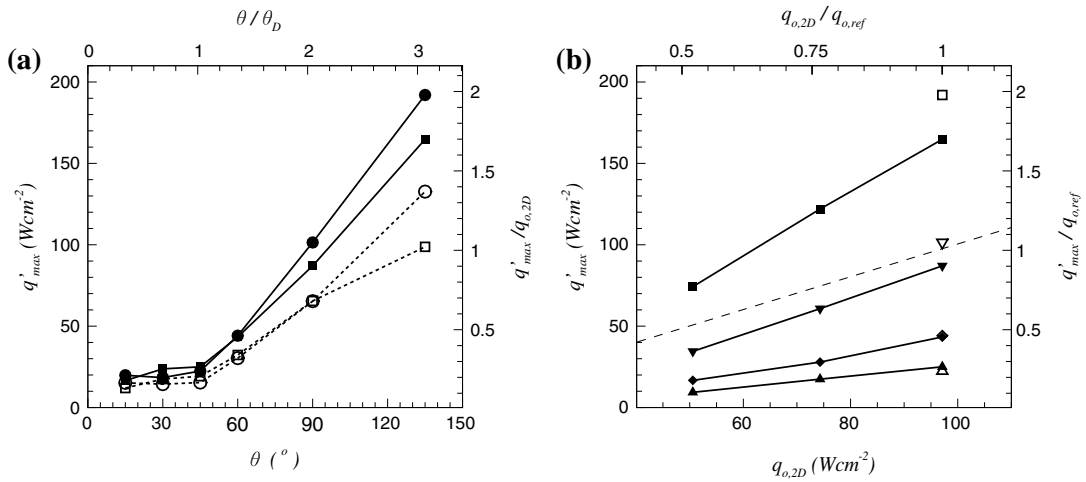

Fig. 13 Heat transfer at peak heating location with incoming laminar boundary layer ($\bar{q}_{\max}$ *open circle symbol*, $q'_{\max}$ *filled circle symbol*) and turbulent boundary layer ($\bar{q}_{\max}$ *open square symbol*, $q'_{\max}$ *filled square symbol*) at $M_\infty = 8.2$ and $Re_\infty/m = 9.35 \times 10^6$ (**a**), and experimental $q'_{\max}$ compared with theoretical prediction for cases $\theta = 45°$ (*filled triangle symbol*), $\theta = 60°$ (*filled diamond symbol*), $\theta = 90°$ (*filled inverted triangle symbol*) and $\theta = 135°$ (*filled square symbol*) based on Eq. 1 for different Re_∞/m conditions at $M_\infty = 8.2$ (respectively, *open triangle symbol*, *open diamond symbol*, *open inverted triangle symbol* and *open square symbol* for laminar flow); dashed line indicates $q'_{\max} = q_{o,2D}$ (**b**)

heat transfer relations deriving from the work of Fay and Riddell (1958) and Kemp et al. (1959). For 2D configurations, and based on the peak heating at R_1 over tall cylindrical obstacles, Crabtree et al. (1970) bring forward the following relation:

$$q_{o,2D} = \frac{0.564}{Pr^{0.6}} (\rho_{o,e}\mu_{o,e})^{0.42} (\rho_w \mu_w)^{0.08} c_p (T_o - T_w)\beta \qquad (1)$$

with Prandtl number $Pr = 0.72$, specific heat $c_p = 1004.5\,\mathrm{J/(kg\,K)}$ and $\beta = \sqrt{(\mathrm{d}u_e/\mathrm{d}x)_o}$, where stagnation velocity gradient assumes Newtonian flow and is based on the shortest length scale, most commonly diameter but here $(\mathrm{d}u_e/\mathrm{d}x)_o = (1/h)\sqrt{2(P_{o,e} - p_\infty)/\rho_{o,e}}$ for shallow obstacles, where subscripts 'o,e' indicate stagnation conditions at boundary layer edge behind a normal shock.

The $\bar{q}_{\max}$ and $q'_{\max}$ levels for the complete range of deflection angles at $M_\infty = 8.2$ and $Re_\infty/m = 9.35 \times 10^6$ are presented in Fig. 13a, with $\bar{q}_{\max}$ being generally at the same level for laminar and turbulent flow (except for $\theta = 135°$) but with $q'_{\max}$ particularly reflecting the transient increase of order ~15 % in peak heating above the fully turbulent levels. This effect is attributed to the relatively larger eddies and organised turbulent structures which lead to enhanced transient heating effects in transitional interactions (Hillier et al. 2015). The peak heat transfer rates for $\theta = 90°$ obstacles are of the order of the peak heating estimated at $R_1 (\sim q_{o,2D})$, with rates almost twice as high measured in the forward deflection cases ($\theta = 135°$). While the peak heating at R_1 cannot be provided with certainty in part due to the assumptions in the velocity gradient term (short height, wall-bounded flow), it is unlikely to be significantly higher than that at R_2 considering that $q'_{\max}$ in the latter cases is even in excess of the stagnation heating over a 5-mm-radius hemispherical nose ($q_{o,N}$ where $r = h$) as determined in the preliminary stages of the investigation (Sect. 2). Unlike in tall cylinder and blunt fin interactions, whereby the extreme heating rates are often attributed to the supersonic jet resulting from the interaction between the separation shock and the bow shock (clearly distanced from the obstacles here), it rather appears that for the present short obstacles it is the reattachment of the separated shear layer itself which results in the extreme heat transfer rates. Either way, the nature of the heat transfer mechanisms at R_1 and R_2 appears to be dominated by stagnation effects, the stagnation streamline in the latter having also gone through the bow shock (Fig. 10b).

In Fig. 13b, the correlation with $q_{o,2D}$ is shown to persist for the different flow conditions and ramp angles for cases greater than the inviscid detached shock angle $\theta > \theta_D$. While this is in part exaggerated by the reduced thermal potential $\Delta T = (T_o - T_w)$ at lower Re_∞ (about 25 % lower than at the highest Re_∞), $q'_{\max}$ variations across the different cases are significantly greater than this and the scaling with $q_{o,2D}$ seems to be consistent (note momentum variations are inherently accounted for as well). It also appears highly unlikely that the consistency in the trends would be an artefact of a systematic underprediction in the form of a similar near-miss of the reattachment across all the different cases so that this also serves to consolidate that the

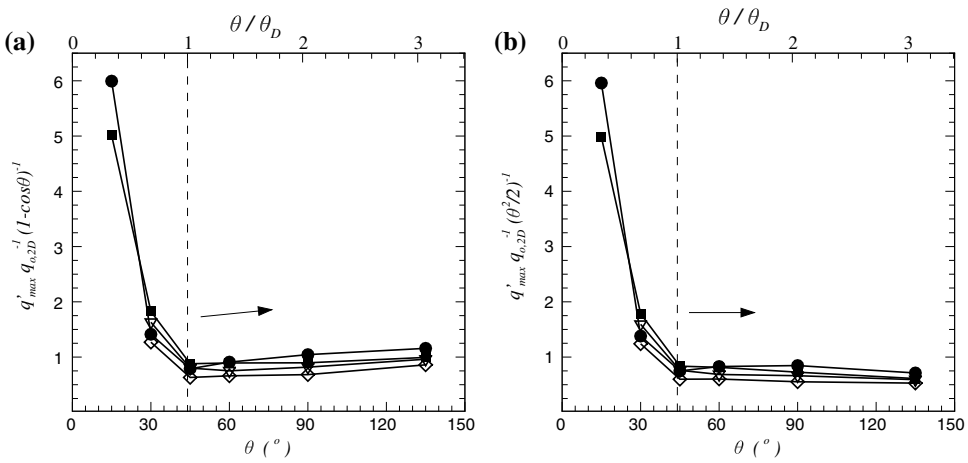

Fig. 14 Peak heat transfer rates $q'_{\max}$ at all $M_\infty = 8.2$ conditions based on Eq. 2: with $(1 - cos\theta)$ term (**a**) and with $(\theta^2/2)$ term (**b**). Symbols as per Fig. 12; *dashed line* and *arrow* indicate blunt ramp regime $\theta/\theta_D > 1$ and correlation tendency

peak heat transfer rates are rightly captured by $q'_{\max}$. Further comparison of the $\theta = 135°$ data in Figs. 9a and 13a clearly shows that the evaluation of $q'_{\max}$ instead of the mean at the maximum heating location $\bar{q}_{\max}$ does capture the highly localised and unsteady peak heat transfer rates expected in between the two counter-rotating vortices ahead of the obstacle, R_2 thus being intermittently measured at the sensor location.

Taking $q_{o,2D}$ for the $\theta = 90°$ case as a reference, and as per earlier observations in Estruch-Samper et al. (2010), $q'_{\max}$ can be shown to correlate with $(1 - \cos\theta)$ for $\theta > \theta_D$ across all the different test conditions (Fig. 14a). From an order of magnitude perspective, further inspection suggests that this term—originally considered to account for relative variations in deflection angle with respect to $\theta = 90°$—may be simplified through trigonometric approximation to $\theta^2/2$, so that as shown in Fig. 14b:

$$q'_{\max} \approx \phi_1 q_{o,2D}(1 - \cos\theta) \approx \phi_1 q_{o,2D}(\theta^2/2) \tag{2}$$

where term ϕ_1 is a function of other flow variables and is approximately $\phi_1 \approx 1$ at $M_\infty = 8.2$ and $\phi_1 \approx 0.5$ at $M_\infty = 12.3$.

Despite the $(1 - \cos\theta) = 0.5\theta^2$ identity deriving from small angle approximations, variations within the upper range of angles are relatively low in comparison with the overwhelming increase in $q'_{\max}$ and in fact result in a slightly enhanced fit to the trend with the latter (Fig. 14b).

As a further check, and noting the potential influence of the bow shock for blunt ramps ($\theta > \theta_D$), the pressure to heat transfer relation from Coleman and Stollery (1972) is evaluated at the stagnation pressure behind a normal shock, $P_{o,N}$. Defining the ratios with respect to undisturbed flow conditions, $P_{o,R} = P_{o,N}/p_u$ and $Q_{\max,R} = q'_{\max}/q_u$, and through Reynolds analogy:

$$Q_{o,R} = \frac{\kappa}{P_{o,R} + 6} \frac{[M_\infty^2 P_{o,R}(P_{o,R} + 6)]^{0.65}}{[\kappa M_\infty^2 - 5(P_{o,R}^2 - 1)]^{0.15} M_\infty \kappa^{0.5}} \tag{3}$$

where $\kappa = 6P_{o,R} + 1$.

Taking into account the effect of deflection angle in Eq. 2, the peak heat transfer rates over the surface ahead of ramp obstacles can be considered:

$$Q_{\max,R} \approx \phi_2 Q_{o,R}(\theta^2/2) \approx \phi_2 P_{o,R}^{0.85}(\theta^2/2) \tag{4}$$

where in this instance $\phi_2 \approx \phi_1$.

Evaluation of the complete experimental $q'_{\max}$ dataset with the respective predictions is presented in Fig. 15, together with some of the earlier mentioned studies on 2D and axisymmetric interactions (Sect. 1) in order to explore potential associations with more widely investigated low-deflection SBLIs ($\theta < \theta_D$). Further inspection in fact shows that Eq. 3 yields very similar results to the more generic power–law relationship $Q_{\max,R} = P_{o,R}^{0.85}$ (Back and Cuffel 1970) and may offer some form of theoretical reasoning behind its applicability in cold wall hypersonic flows, both estimates being within 8 % agreement from each other for all the cases in the figure except at the higher Mach number of 11.3–11.4 where the latter relation yields 14 % higher values. As shown in the figure, the peak heating ahead of ramp obstacles is found to scale reasonably well with $P_{o,N}$ (Eq. 4), whereby $P_{o,\infty}$ is effectively doubled across the present range (Table 1). It is noted that comparison is not straightforward given the peak heating in the reference interactions in the figure corresponds instead to the primary reattachment for lower-deflection ramps. In such cases, the stagnation streamline is not further compressed through the bow shock and the total pressure at reattachment is greater

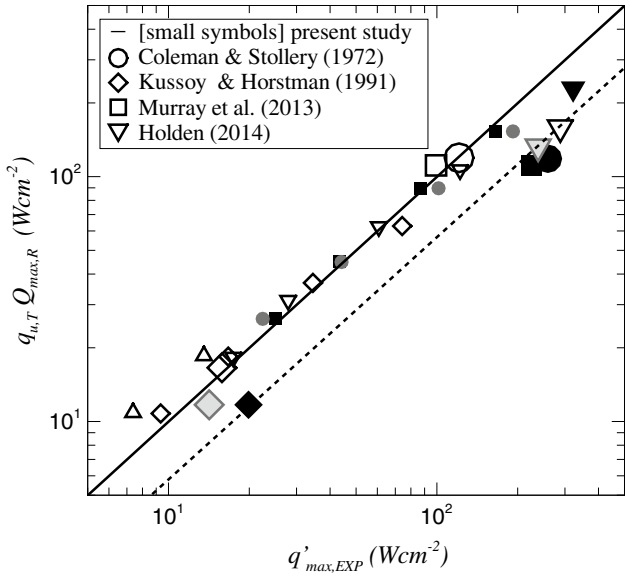

Fig. 15 Evaluation of predictions based on Eq. 4 with present results (small symbols as per Fig. 12) and results from Coleman and Stollery (1972): Mach 9.22, 30° incipient 2D ramp (*open circle symbol*) and Mach 9.22, 38° 2D ramp (*filled circle symbol*); Kussoy and Horstman (1991): Mach 8.18, 10° 2D impinging shock (*open diamond symbol*), Mach 7.05, 30° incipient axisymmetric ramp (*grey open diamond symbol*) and Mach 7.05, 35° axisymmetric ramp (*filled diamond symbol*); Murray et al. (2013): Mach 8.9, 10° axisymmetric impinging shock (*open square symbol*) and Mach 8.9, 30° axisymmetric ramp (*filled square symbol*); Holden (2014): Mach 11.4, 20° 2D impinging shock (*open inverted triangle symbol*), Mach 11.3, 26° 2D ramp (*grey inverted triangle symbol*) and Mach 8.2, 36° 2D ramp (*filled inverted triangle symbol*). *Solid and dashed lines* indicate $q_{u,T}Q_{\max,R} = q'_{\max,EXP}$ and offset for reference SBLIs with separation

than $P_{o,N}$, thus leading to higher $q'_{\max}$ values than predicted with Eq. 3 (dashed line in Fig. 15). In incipient interactions, the local maximum appears to be more closely related to $P_{o,N}$, suggesting its suitability as a parameter for incipient separation relations as for instance assumed in Zheltovodov (1996), where it is equated to plateau pressure as an incipience criteria.

A simple evaluation of existing correlations shows that the relation $q_{\max}/q_u = 1 + 25M^{1.8}Re_x^{-0.2}$ in Tang and Yu (1992) overpredicts the present measurements by over a factor of 4 ($M = 8.2$) and up to well over an order of magnitude at the highest Mach number ($M = 12.3$). Further evaluation with the relation of Neumann and Hayes (1981), $q_{\max}/q_u = (0.92 + 1.1M^{1.5})(T_o - T_w)/(T_{aw} - T_w)$ instead shows that the present Mach 8.2 data is underpredicted by about 2 times and the Mach 12.3 is overpredicted by 5 times. Another relation is that by Neumann and Hayes (1986), $q_{\max} = 2.41 \times 10^{-3} M_e P_{o,N}^{0.9735}(0.9T_o - T_w)$ [in S.I. units], which results from a re-evaluation of the data in Neumann and Hayes (1981) and includes also that in Winkelmann (1972), Hung and Barnett (1973) as well as other unpublished AFFDL results. This relation instead finds very good agreement with the present Mach 12.3 data but underpredicts the Mach 8.2 data by a factor of 2.8 (note some of the assumptions vary amongst relations, e.g. the simple scaling with Mach number in the latter). In the same manner, when evaluated against other data in the literature, the relation in the study preceding this paper (Estruch-Samper et al. 2010), which was directly correlated through Buckingham-Pi analysis as $q_{\max} = 0.52(\rho_e U_e) Re_h^{0.6} M_e^{-0.5}(1 - \cos\theta)c_p(T_o - T_w)$ [in W/m^2], may also be found to result in significant differences when extrapolated to very different flow conditions, e.g. significantly overpredicting the Mach 5 cylinder data of Neumann and Hayes (1981) yet with closer agreement in other cases (e.g. in Kumar and Reddy 2013, 2014 for similar conditions). This therefore highlights the restricted applicability of such approaches.

While the modelling of flow stagnation effects upon reattachment is highly complex and influenced by a wide array of parameters, the present results do evidence a strong association between stagnation and peak heating and hence suggest the problem is dominated by inviscid terms. In more recent experiments using thermographic imaging, Neumann and Freeman (2012) further highlight the strong gradients in recovery temperature upstream of protuberances, which vary significantly through the separation and reach maximum values of order $T_r \approx 0.98$–0.99, so that the assumption of $T_r \approx T_o$ appears appropriate for peak heating correlations. From a more fundamental standpoint, and assuming that $q'_{\max}$ is induced by the conversion of kinetic energy into heat with minor viscous dissipation, it may therefore be concluded that the prevailing aspect associated with the peak heating upstream of the present obstacles is the stagnation of the flow, with the additional effects of boundary layer state, Reynolds and Mach number (among other factors) influencing the problem to a lesser extent.

3.3 Effect of deflection angle

As explained through free-interaction theory, the separation of the boundary layer is essentially driven by the incoming flow conditions so that the streamwise pressure gradient through the separation shock and the normal shear stress gradient at the wall are $\mathrm{d}p/\mathrm{d}x = (\mathrm{d}\tau/\mathrm{d}y)_w$. By integrating along the separation region, the boundary layer response can be expressed as a function of the total adverse pressure gradient normalised by dynamic pressure q_o, separation length L, boundary layer thickness δ_o and skin friction coefficient $C_{f,o} = \tau_{w,o}/q_o$:

$$C_{f,o}\frac{L}{\delta_o} \propto \frac{p - p_o}{q_o} \tag{5}$$

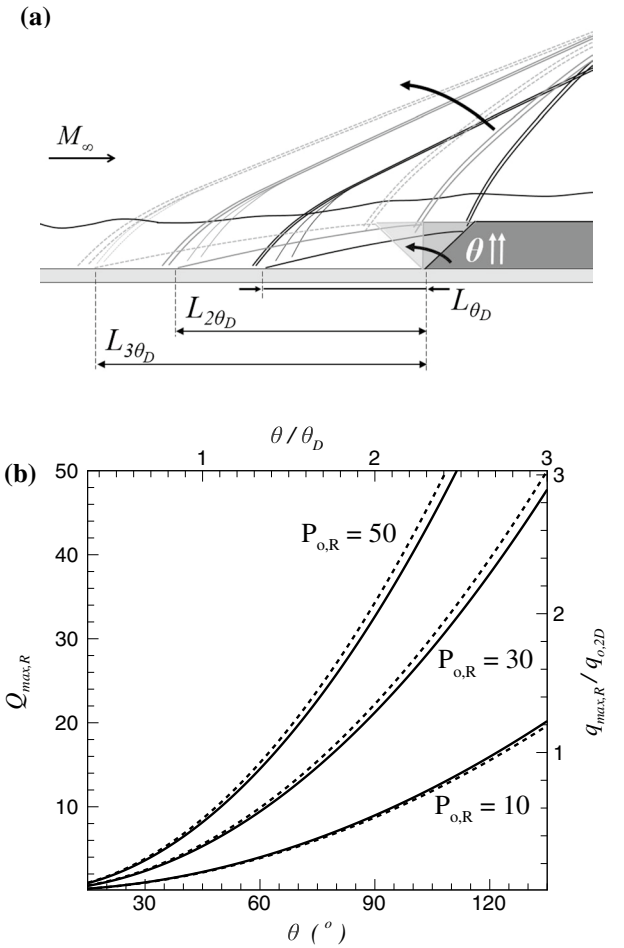

Fig. 16 Schematic of interactions depicting effect of deflection angle (**a**) and $Q_{\max,R}$ at $M_\infty = 8.2$, $Re_\infty/m = 9.35 \times 10^6$ conditions for $P_{o,R} = 10$, $P_{o,R} = 30$ and $P_{o,R} = 50$ with dashed line based on $Q_{o,R}$ form of Eq. 4 and *solid line* based on $P_{o,R}^{0.85}$ form, both assuming $\phi_2 = 1$ (**b**)

Through inviscid theory, for a supersonic simple wave flow, the adverse pressure gradient is then assumed proportional to flow deflection angle $\Delta\theta$ in the form:

$$\frac{p - p_o}{q_o} \propto \frac{1}{\sqrt{M^2 - 1}} \Delta\theta \tag{6}$$

For high Mach number flow and noting that $q_o = 0.5\gamma p_o M_o^2$, the pressure jump simplifies to $p/p_o \sim K$, where $K = M\theta$ is the hypersonic similarity parameter. While this parameter is more often used to characterise the pressure rise across oblique shock problems, linearised theory assumptions reduce it in such cases to high Mach number and small angle simplifications (e.g. tangent-wedge theory for slender bodies). As a result, the dominant effect of ramp angle for angles $\theta \geqslant 45°$ cannot be understood to be directly associated with an increase in shock strength by itself.

On the other hand, $K = M\theta$ is also the hypersonic limit for the pressure jump given by the linearised Prandtl–Meyer law (Anderson 2000), for which small angle simplifications are not involved:

$$-\frac{p - p_o}{q_o} \propto (M\Delta\theta)^2 \tag{7}$$

and where $\Delta\theta$ is here the expansion angle. The hypersonic similarity parameter $K = M\theta$ is experimentally validated for both hypersonic compression and expansion problems (Stollery and Bates 1974), yet at significantly lower angles than those considered here.

As per Fig. 14, the present dependence on θ for angles well in excess of the inviscid detached shock condition suggests that the increasing extent of the separation is driven by the influence of the expansion of the flow at the trailing edge of the compression surface, i.e. near the top lip of the obstacle, through an upstream feedback mechanism similar to that described in Hunter and Reeves (1971) for compression–decompression configurations with short compression surface length. As per the schematic in Fig. 10b, the upstream influence of the rapid boundary layer expansion at the top edge of the obstacle is communicated through the subsonic region of the interaction. This effect is restricted to short obstacles whereby reattachment occurs near the top edge and where the downstream relaxation of the boundary layer has to accommodate the abrupt expansion in the region (Roshko and Thomke 1976). Such an upstream feedback mechanism is not encountered in long compression ramps or taller obstacles whereby the 'sonic throat' downstream of reattachment is located over the compression surface, i.e. well upstream of the top edge (Zheltovodov 1996, 2006).

Through turbulent flow assumptions, a direct combination of Eqs. 5 and 6 would suggest that the interaction length scales approximately as $L/\delta \propto Re_x^{0.2} M_o^{-1}\theta$, for weak interactions with viscous and inertia forces of a similar magnitude (note free-interaction assumptions prime viscous effects). For strong interactions, whereby the inviscid terms are significantly greater than the viscous terms, the relevance of the hypersonic similarity parameter increases accordingly (Stollery 1970) so that, as further mentioned in Délery and Marvin (1986) and Arnal and Délery (2004), the extent of the separation scales as:

$$\frac{L}{\delta_o} \propto \frac{(M_o\theta)^2}{\bar{\chi}_s} \tag{8}$$

where $\bar{\chi}_s$ is the strong viscous term and the $M\theta$ product here manifests the dominant effect of the expansion region over the top edge of the obstacle (Eq. 7).

For turbulent flow, and with reference to local flow conditions, Stollery and Bates (1974) define:

$$\bar{\chi}_s = \left(\frac{C_\infty M_\infty^9}{Re_x}\right)^{2/7} \tag{9}$$

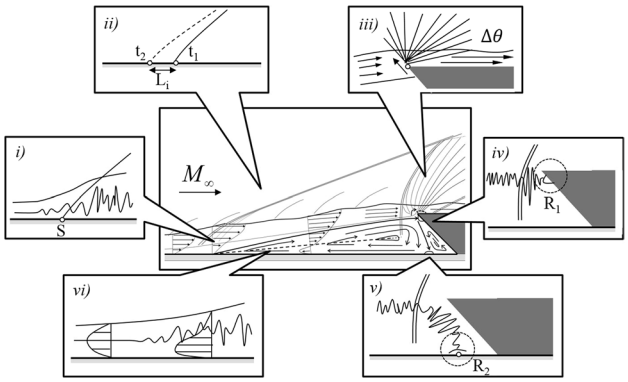

Fig. 17 Summary of main features in short blunt obstacles (schematic based on $\theta = 135°$ case with incoming laminar flow)

where C_∞ is the Chapman–Rubesin parameter $C_\infty = (\mu/\mu_\infty)/(T/T_\infty)$. The separation length relation in Eq. 8 thus becomes:

$$\frac{L}{\delta_o} \propto Re^{2/7} M^{-4/7} \theta^2 \tag{10}$$

While in practice the effect of Reynolds and Mach number on separation length varies significantly across the literature, with correlations such as for instance $L/\delta_o = (\theta/18.25)^{2.81}[10^3 C_{fo} - 1 + (\theta/29)^2]$ in Roshko and Thomke (1976) and $L/\delta_o = Re^{-0.36}\, 0.9e^{0.23\theta}$ in Settles and Bogdonoff (1982), the exponential increase in separation length with deflection angle is well established to scale proportionally with mass flow deficit ratio across the interaction (Souverein et al. 2013) and is thus to some extent sensitive to the fraction of low momentum flow bled to the sides of the obstacle (and hence width).

Eventually, the competing effect between the 'strong inviscid term' $(M_o\theta)^2$ and the 'strong displacement term' $\bar{\chi}_s$ leads to a much weaker influence of Reynolds and Mach number in contrast to that of deflection angle (Stollery and Bates 1974). As interpreted in Fig. 16a, the consequent increase in separation length with θ results in a longer distance (or mixing length) required by the separated shear layer to accelerate under the action of viscous forces and eventually attain sufficient momentum to overcome the obstacle (Délery and Marvin 1986). In this manner, peak heating rates are shown to vary accordingly as a function of the higher mass flow deflection and subsequent increase in separation length, with $q'_{\max}$ increasing exponentially with ramp angle (Fig. 16b).

Overall, bearing in mind the complex nature of 3D SBLIs, the brief assessment in this paper aims at evaluating a relatively substantial dataset—covering a rarely documented range of ramp angles—against basic physical assumptions. While contemplated from a broad approach, results demonstrate a strong influence of stagnation effects (with different degrees of relevance from case to case) but with a particularly high sensitivity to deflection angle in comparison with the generally lower effect of other parameters so that, in fundamental terms, the maximum heat transfer can be more widely regarded to scale as:

$$q'_{\max} \propto q_{o,2D}\theta^2 \tag{11}$$

In Fig. 17, and complementing the main phenomena highlighted in Knight and Zheltovodov (2014) for compression–decompression ramps geometries with reattachment well upstream of the edge (i.e. for taller configurations), the main features in short blunt obstacle SBLIs are summarised as follows: (i) laminar-turbulent transition and/or enhancement of incoming turbulent fluctuations near separation, (ii) intermittent separation over a distance L_i marked by low-frequency large-scale unsteadiness, (iii) abrupt expansion at top edge (within relaxation region), (iv) stagnation upon primary reattachment on obstacle's front face, (v) stagnation upon secondary reattachment on surface ahead of obstacle and (vi) upstream feedback of turbulent disturbances approaching separation. The dominant influence of the flow at the top edge of the obstacle is proven to be inherent to obstacle heights of order of the boundary layer thickness or shorter, whereby the location of reattachment is fixed close ahead of the edge and where the subsequent relaxation region must compensate for the abrupt expansion at the obstacle's height through increased separation extent. Besides the implications on the local heating augmentation, the strong sensitivity of the separation bubble to the flow near the top leading edge region is expected to also play a key role in roughness-induced transition and micro-vortex generator control problems (Fiala et al. 2014; Estruch-Samper et al. 2015), where local interference effects can have a major downstream influence.

4 Conclusions

The heat transfer effects in hypersonic SBLIs induced by short ramp obstacles have been investigated. An assessment into the nature of the maximum heat transfer rates suggests they are strongly influenced by the stagnation of the flow upon reattachment. Peak heating levels are found to be particularly sensitive to ramp angle, with the resulting strengthening of the separated shear layer leading to peak heat transfer rates scaling as $q'_{\max} \propto q_{o,2D}\,\theta^2$.

The dominant effect of deflection angle all the way up to $\theta = 135°$ is associated with the rapid expansion of the boundary layer just downstream of primary reattachment at the top edge of the obstacle, which is communicated

upstream causing an increase in the extent of the separation to satisfy momentum balance. The longer separation length in turn leads to the strengthening of the reattaching shear layer and subsequent increased heating upon its stagnation.

Acknowledgments The author would like to gratefully acknowledge the support of the several technical and academic staff members at the College of Aeronautics, Cranfield University, who helped in the earlier stages of the study and the kind advise of the late Prof. Em. John L. Stollery. The continued support of the Ministry of Education (MOE) Singapore through AcRF Tier 1 R-265-000-482-133 is also acknowledged.

References

Anderson JD (2000) Hypersonic and high temperature gas dynamics. AIAA Education Series, American Institute of Aeronautics and Astronautics, USA

Arnal D, Délery J (2004) Laminar-turbulent transition and shock wave/boundary layer interaction. NATO RTO-EN-AVT-116, pp 4.1–4.46

Avallone F, Ragni D, Schrijer FFJ, Scarano F, Cardone G (2015) PIV-based study of a cylindrical roughness element in a hypersonic laminar boundary layer. In: 11th international symposium particle image velocimetry PIV15

Babinsky H, Harvey JK (2014) Shock wave-boundary-layer interactions. Cambridge Aerospace Series, Cambridge University Press, Cambridge

Back LH, Cuffel RF (1970) Changes in heat transfer from turbulent boundary layers interacting with shock waves and expansion waves. AIAA J 8:1871–1873

Chapman DR, Kuehn DM, Larson HK (1957) Investigation of separated flows in supersonic and subsonic streams with emphasis on the effect of transition. NACA TN-3869, pp 421–460

Clemens NT, Narayanaswamy V (2014) Low-frequency unsteadiness of shock-wave/turbulent boundary layer interactions. Ann Rev Fluid Mech 46:469–492

Coleman GT, Stollery JL (1972) Heat transfer from hypersonic turbulent flow at a wedge compression corner. J Fluid Mech 56(4):741–752

Crabtree LF, Dommett RL, Woodley JG (1970) Estimation of heat transfer to flat plates, cones and blunt bodies. Aero. Res. Council R.&M, No 3637

Délery J, Marvin JG (1986) Shock wave/boundary layer interactions. AGARDograph No. 280, pp 1–216

Dolling DS (1982) Comparison of sharp and blunt fin-induced shock-wave/turbulent boundary-layer interactions. AIAA J 20(10):1385–1391

Dolling DS (2001) Fifty years of shock-wave/boundary-layer interaction research: what next? AIAA J 39(8):1517–1531

Dupont P, Haddad C, Ardissone JP, Debiève JF (2005) Space and time organization of a shock wave/turbulent boundary layer interaction. Aerosp Sci Technol 9(7):561–572

Elfstrom GM (1973) Turbulent hypersonic flow at a wedge-compression corner. J Fluid Mech 53(1):113–127

Estruch-Samper D, Macmanus D, Stollery J, Lawson N, Garry K (2010) Hypersonic interference heating in the vicinity of surface protuberances. Exp Fluids 49(3):683–699

Estruch-Samper D, Vanstone L, Ganapathisubramani B, Hillier R (2015) Micro vortex generator control of axisymmetric high-speed laminar boundary layer separation. J Shock Waves 25(5):521–533

Fay JA, Riddell FR (1958) Theory of stagnation point heat transfer in dissociated air. J Aerosp Sci 25(2):73–85

Fiala A, Hillier R, Estruch-Samper D (2014) Roughness-induced turbulent wedges in a hypersonic blunt body boundary layer. J Fluid Mech 754(9):208–231

Gnoffo PA, Berry SS, van Norman JW (2013) Uncertainty assessments of 2D and axisymmetric hypersonic shock wave-turbulent boundary layer interaction simulations at compression corners. J Spacecr Rockets 50(1):69–95

Hahn M (1969) Experimental investigation of turbulent step-induced boundary-layer separation at Mach numbers 2.5, 3 and 4. AEDC-TR-69-1, pp 1–31

Hillier R, Estruch-Samper D, Murray N, Vanstone L, Williams S (2015) Gun tunnel studies of shock-wave/boundary-layer interactions: laminar, transitional and turbulent, John Stollery Lecture, 20th AIAA international space planes and hypersonic systems and technologies conference, AIAA paper 2015-3512

Holden MS (2014) Experimental studies of shock-wave-boundary-layer interactions in hypersonic flows. In: Babinsky H, Harvey JK (eds) Cambridge aerospace series: shock wave–boundary-layer interactions, chap 6. Cambridge University Press, Cambridge

Hung FT, Barnett DO (1973) Shock wave-boundary layer interference heating analysis. In 11th AIAA aerospace science meeting, AIAA paper 73-237

Hung FT, Patel D (1984) Protuberance interference heating in high-speed flow. In 19th AIAA thermophysics conference, AIAA paper 84-1724

Hunter LG, Reeves BL (1971) Results of a strong interaction, wake-like model of supersonic separated and reattaching turbulent flows. AIAA J 9(4):703–712

Jones RA (1964) Heat-transfer and pressure investigation of a fin-plate interference model at a Mach number of 6. NASA TN D-2028

Kemp NH, Rose PH, Detra RW (1959) Laminar heat transfer around blunt bodies in dissociated air. J Aerosp Sci 26(7):421–430

Knight D, Longo J (2012) Assessment of aerothermodynamic flight prediction tools through ground and flight experimentation, chapter 2: shock interactions and control surfaces. NATO RTO-TR-AVT-136, 2, pp 1–36

Knight D, Zheltovodov A (2014) Ideal-gas shock wave-turbulent boundary-layer interactions (STBLIs) in supersonic flows and their modeling: two-dimensional interactions. In: Babinsky H, Harvey JK (eds) Cambridge aerospace series: shock wave–boundary-layer interactions, chap 4. Cambridge University Press, Cambridge

Kumar K, Reddy KPJ (2013) Experimental investigation of heat fluxes in the vicinity of protuberances on a flat plate at hypersonic speeds. J Heat Transf 135: 121701 1–9

Kumar K, Reddy KPJ (2014) Hypersonic interference heating on flat plate with short three-dimensional protuberances. AIAA J 52(4):747–756

Kussoy MI, Horstman KC (1991) Documentation of two- and three-dimensional shock-wave/turbulent-boundary-layer interaction flows at Mach 8.2. NASA TM-103838

Marvin JG, Brown JL, Gnoffo PA (2013) Experimental database with baseline CFD solutions: 2-D and axisymmetric hypersonic shock-wave/turbulent-boundary-layer interactions. NASA TM-2013-216604

Mohammadian S (1972) Viscous interaction over concave and convex surfaces at hypersonic speeds. J Fluid Mech 55(1):163–175

Murray N, Hillier R, Williams S (2013) Experimental investigation of axisymmetric hypersonic shock-wave/turbulent-boundary-layer interactions. J Fluid Mech 714:152–189

Needham DA (1963) Progress report on the Imperial College hypersonic gun tunnel. Imperial College of Science and Technology, Report No 118

Needham DA, Stollery JL (1966) Hypersonic studies of incipient separation and separated flows. AGARD CP 4(I):89–119

Nestler DE (1985) The effects of surface discontinuities on convective heat transfer in hypersonic flow. In: 20th AIAA thermophysics conference, AIAA paper 85-0971

Neumann RD, Hayes JR (1981) Protuberance heating at high Mach numbers, a critical review and extension of the database. In: 20th AIAA thermophysics conference, AIAA paper 81-0420

Neumann RD, Hayes JR (1986) Introduction to aerodynamic heating analysis of supersonic missiles. In: Hemsch M, Nielsen J (eds) AIAA progress in astronautics and aeronautics: tactical missile aerodynamics, vol 104. AIAA, New York, pp 421–481

Neumann RD, Freeman DC (2012) Experimental measurement of aerodynamic heating about complex shapes at supersonic Mach numbers. J Spacecr Rockets 49(6):1080–1087

Oldfield MLG, Jones TV, Schultz DL (1978) On-line computer for transient turbine cascade instrumentation. IEEE Trans Aerosp Electron Syst AES 14(5):738–749

Ozcan O, Holt M (1984) Supersonic separated flow past a cylindrical obstacle on a flat plate. AIAA J 25(5):611–617

Reshotko E (2008) Transition issues for atmospheric re-entry. J Spacecr Rockets 45(2):161–164

Roshko A, Thomke GL (1976) Flare-induced interaction length in supersonic, turbulent boundary layers. AIAA J 14(7):873–879

Schlamp S, Prochazka L, Rosgen T (2007) Shock wave/boundary layer interaction experiment on control surface. NATO RTO-EN-AVT-130, 14, pp 1–22

Schneider SP (2008) Effects of roughness on hypersonic boundary-layer transition. J Spacecr Rockets 45(2):193–209

Schultz DL, Jones TV (1973) Heat-transfer measurements in short-duration hypersonic facilities. AGARDograph 165

Sedney R (1973) A survey of the effect of small protuberances on boundary layer flows. AIAA J 11(6):782–792

Sedney R, Kitchens CW (1977) Separation ahead of protuberances in supersonic turbulent boundary layers. AIAA J 15(4):546–552

Settles GS, Bogdonoff SM, Vas LE (1976) Incipient separation of a supersonic turbulent boundary layer at high Reynolds numbers. AIAA J 14(1):50–56

Settles GS, Bogdonoff SM (1982) Scaling of two- and three-dimensional shock/turbulent boundary-layer interactions at compression corners. AIAA J 20(6):782–789

Souverein LJ, Bakker PG, Dupont P (2013) A scaling analysis for turbulent shock-wave/boundary-layer interactions. J Fluid Mech 714:505–535

Stollery JL (1970) Hypersonic viscous interaction on curved surfaces. J Fluid Mech 43(3):497–511

Stollery JL, Bates L (1974) Turbulent hypersonic viscous interaction. J Fluid Mech 63(1):145–156

Tang G (1998) Heating characteristics of blunt swept fin-induced shock wave turbulent boundary layer interaction. Acta Mech Sin 14(2):139–146

Tang GM, Yu HR (1992) Aerodynamic heating in the region of shock and turbulent boundary layer interaction induced by a cylinder. Acta Mech Sin 8(3):224–230

Token KH (1974) Heat transfer due to shock wave turbulent boundary layer interactions on high speed weapon systems. Air Force Flight Dynamics Laboratory AFFDL Report TR-74-77, pp 1–114

Winkelmann AB (1972) Experimental investigations of a fin protuberance partially immersed in a turbulent boundary layer at Mach 5. Naval Ordnance Lab. TR-72-33, pp 1–120

Zheltovodov AA (1996) Shock waves/turbulent boundary-layer interactions: fundamental studies and applications. In: 27th AIAA fluid dynamics conference, AIAA paper 96-1977

Zheltovodov AA (2006) Some advances in research of shock wave turbulent boundary-layer interactions. In: 44th AIAA aerospace science meeting and exhibit, AIAA paper 2006-0496